

# Bayesian Neural Networks for Virtual Flow Metering: An Empirical Study

Bjarne Grimstad<sup>a,b,\*</sup>, Mathilde Hotvedt<sup>a,b</sup>, Anders T. Sandnes<sup>a,c</sup>, Odd  
Kolbjørnsen<sup>c</sup>, Lars S. Imsland<sup>b</sup>

<sup>a</sup>*Solution Seeker AS, Oslo, Norway*

<sup>b</sup>*Department of Engineering Cybernetics, Norwegian University of Science and Technology,  
Trondheim, Norway*

<sup>c</sup>*Department of Mathematics, University of Oslo, Oslo, Norway*

---

## Abstract

Recent works have presented promising results from the application of machine learning (ML) to the modeling of flow rates in oil and gas wells. The encouraging results combined with advantageous properties of ML models, such as computationally cheap evaluation and ease of calibration to new data, have sparked optimism for the development of data-driven virtual flow meters (VFMs). We contribute to this development by presenting a probabilistic VFM based on a Bayesian neural network. We consider homoscedastic and heteroscedastic measurement noise, and show how to train the models using maximum a posteriori estimation and variational inference. We study the methods by modeling on a large and heterogeneous dataset, consisting of 60 wells across five different oil and gas assets. The predictive performance is analyzed on historical and future test data, where we achieve an average error of 5-6% and 9-13% for the 50% best performing models, respectively. Variational inference appears to provide more robust predictions than the reference approach on future data. The difference in prediction performance and uncertainty on historical and future data is explored in detail, and the findings motivate the development of alternative strategies for data-driven VFM.

*Keywords:* Neural Network, Bayesian Inference, Variational Inference, Virtual Flow Metering, Heteroscedasticity

---

## 1. Introduction

Knowledge of multiphase flow rates is essential to efficiently operate a petroleum production asset. Measured or predicted flow rates provide situational awareness and flow assurance, enable production optimization, and improve reservoir management and planning. However, subsurface fluid properties are uncertain

---

\*Corresponding author

*Email address:* bjarne.grimstad@gmail.com (Bjarne Grimstad)

and multiphase flow dynamics is complex, making multiphase flow rates challenging to obtain with great accuracy [1]. In most production systems, flow rates are measured using well testing. While these measurements are of high accuracy, they are intermittent and infrequent [2]. Some production systems have multiphase flow meters (MPFMs) installed at strategic locations to continuously measure flow rates, yet, these devices are expensive and typically have lower accuracy than well testing. Another approach to obtaining the flow rates is through virtual flow metering (VFM). VFM is a soft-sensing technology that predicts the flow rates in the production system using a mathematical model and existing measurements [3]. Many fields today use some form of VFM technology complementary to flow rate measurements. There are two main applications of a VFM: 1) real-time prediction of flow rates and 2) prediction of historical flow rates. The second application is relevant to the prediction of missing measurements due to sensor failure or lacking measurements in between well tests.

Commonly, VFMs are divided into two fundamental groups; mechanistic and data-driven [4]. Both types may be either dynamic or steady-state. Mechanistic VFM models are derived from prior knowledge about the internal structure of the process [5]. Physical, first-principle laws such as mass, energy, and momentum-balance equations, along with empirical closure relations are utilized to describe the relationship between the system variables. Mechanistic modeling is the most common approach in today’s industry, and some commercial VFMs are Prosper, ValiPerformance, LedaFlow, FlowManager and Olga [6]. In contrary to mechanistic models, data-driven models exploit patterns in process data and attempt to find relationships between the system variables with generic mathematical models, in other words, without explicit prior knowledge about the process [5]. In recent years, there has been an increasing number of data-driven VFMs presented in the literature. The developments are motivated by the increasing amount of sensor data due to improved instrumentation of petroleum fields, better data availability, and more computing power [7]. Additionally, data-driven VFMs typically requires less maintenance than a mechanistic VFMs [8]. Nevertheless, to the authors’ knowledge, commercial data-driven VFMs are practically non-existent.

### 1.1. Data challenges

We consider three prevalent challenges of data-driven modeling that typically decrease VFM performance in a real, industrial scenario:

1. Small data regime
2. Poor measurement quality, such as noisy or biased data
3. Non-stationarity of the underlying process

The first challenge is due to data-driven methods, especially neural networks, being data-hungry, and require substantial data *volume* and *variety* for high accuracy [9]. Yet, petroleum production data do not generally fulfill these requirements. Firstly, production data covers little of the operational region of the production well, resulting in low data variety. Secondly, for petroleum fields

without continuous monitoring of the flow rates, new data is obtained at most 1-2 times per month during well testing [2], yielding low data volume. For fields with continuous measurements, the data volume may be higher, yet, the issue with low variety remain. A common consequence of modeling in the small data regime is overfitting which decreases the generalization ability of the model, that is, the models struggle with extrapolation to unseen operating conditions [5]. Nonetheless, one should be able to model the dominant behavior of the well and make meaningful predictions close to the observed data if care is taken to prevent overfitting [10].

The second challenge, measurement quality, highly influences data-driven VFMs’ predictive abilities as the models are noise sensitive. Unfortunately, many of the measurement sensors in petroleum wells are noisy and biased and may drift or fall out over large periods of time. To improve the quality of data, common practices include preprocessing and data reconciliation [11]. In model development, methods such as parameter regularization and model selection techniques prevent overfitting of the model in the presence of noisy data.

Lastly, the underlying process in petroleum production systems, the reservoir, is non-stationary. The pressure in the reservoir decreases with the reservoir being drained and the composition of the produced fluid changes in time. Therefore, most data-driven VFM will struggle with predicting future process behavior as they often struggle with extrapolation. As above-mentioned, methods to prevent overfitting to the training data in model development may (and should) be utilized to improve extrapolation abilities to the near future, and frequent model updating or online learning would contribute to better predictive abilities for larger changes in the underlying process.

As the above discussion reflects, data-driven VFMs are influenced by uncertainty. Both model (epistemic) uncertainty; the model is not a perfect realization of the true process and there are uncertainties related to the model structure and parameters, and measurement (aleatoric) uncertainty; noisy data due to imprecision in measurements [12]. Accounting for uncertainty is important to the petroleum production engineers as they are often concerned with worst- and best-case scenarios. Further, knowing the prediction uncertainty may aid the production engineers in when the model predictions may be trusted. According to a recent survey [4], it is important that uncertainty estimation is addressed by future research on VFM.

## 1.2. Contributions

We present a probabilistic, data-driven VFM where the flow rate is modeled by a Bayesian neural network, conditioned on available measurements taken at the well. We describe how to accommodate homoscedastic and heteroscedastic measurement noise in the model. Bayesian inference is performed using maximum a posteriori estimation and variational inference. We conduct a large-scale empirical study on a diverse set of 60 petroleum wells *to investigate whether the methods have the performance required of a VFM*. The required performance (on test data) is set to be a mean absolute percentage error of 10% or less [13].

We consider a method to be robust if it achieves this performance on at least 75% of the wells.

In our study, we model the multiphase flow through the production choke valve, a crucial component in any VFM. We consider ideal conditions, in the sense that all measurements required by a reasonable choke model are available. The study is designed to test the predictive performance on historical data and on future data, which reflect the two main applications of a VFM. To cast light on the data challenges in Section 1.1, we differentiate between wells with test separator and MPFM measurements, which have different measurement accuracy and frequency. We also analyze the prediction uncertainty of the models and investigate the effect of training set size on prediction performance.

## 2. Related work

### 2.1. Traditional data-driven modeling

In literature, several data-driven methods have been proposed for VFM modeling, for instance, linear and nonlinear regression, principal component regression, random forest, support vector machines and the gradient boosting machine learning algorithm [14, 15, 16, 17]. One of the most popular and promising data-driven methods for VFM are neural networks (NN). In [14], the oil flow rate from three wells was modeled using NNs, and an error as low as 0.15% was reported. However, well-step tests were used to generate data with sufficient variety, and the time-span of the data covered only 30 hours. The three studies, [18, 19, 20], investigated NNs for the oil flow rate from a reservoir using data samples from 31-50 wells. All used a neural network architecture with one hidden layer and 7 hidden neurons. In the two first, the imperialist competitive algorithm was used to find the NN weights. All of the three studies reported a very small mean squared error, of less than 0.05. Yet, the data was limited to a time-span of 3 months and did not include measurements of the choke openings of the petroleum wells. This will strongly affect the future model performance when reservoir conditions change and the choke openings are adjusted.

A particularly noticeable series of studies on VFM and NN, using historical well measurements with a time-span of more than a year, are [10, 13, 21, 8]. In [13], the oil and gas flow rates were modeled using two individual feed-forward NN, with one hidden layer and 6 and 7 neurons respectively, and with early stopping to prevent overfitting. An error of 4.2% and 2.3% for the oil and gas flow rates were reported. In [8], a radial basis function network was utilized to model the gas flow rate from four gas condensate wells, and the Orthogonal Least Squares algorithm was applied to find the optimal number of neurons ( $\leq 80$ ) in the hidden layer of the network. The study reported an error of 5.9%. In [21, 10], ensemble neural networks were used to excel the learning from sparse data. In the first, the neural network architecture was limited to one hidden layer but the number of hidden neurons was randomly chosen in the range 3-15. Errors of 1.5%, 6.5%, and 4.7% for gas, oil, and water flow rate predictions were achieved. The second paper considered 1-2 hidden layers with

1-25 neurons. Errors of 4.7% and 2.4% were obtained for liquid and gas flow rates respectively.

## 2.2. Probabilistic modeling

A common approach in today’s industry and literature is to study the sensitivity of the model to changes in parameter values, thus to a certain extent approaching epistemic uncertainty, e.g. [22, 23, 14, 24, 2]. By approximating probability distributions for some of the model parameters from available process data and using sampling methods to propagate realizations of the parameters through the model, a predictive distribution of the output with respect to the uncertainty in the parameter may be analyzed.

Probabilistic modeling offers a more principled way to model uncertainty, e.g. by considering model parameters and measurement noise as random variables [25]. With Bayesian inference, a posterior distribution of the model output is found that takes into account both observed process data and prior beliefs of the model parameters [26]. The result is a predictive model that averages over all likely models that fit the data and a model that offers a natural parameter regularization scheme through the use of priors. This is in contrast to traditional data-driven modeling which concern is often to find the maximum likelihood estimate [25]. Although probabilistic models and Bayesian inference are well-known in other fields of research, probabilistic VFMs are rare, yet existent [27, 28, 29, 30].

The following series of studies, [27, 29, 28], constructed a mechanistic, probabilistic model of the flow rate in petroleum wellbores. A method for probabilistic, data-driven models is Bayesian neural networks (BNNs). BNNs are similar to traditional neural networks but with each parameter represented with a probability distribution [26, 31]. Bayesian methods have shown to be efficient in finding high accuracy predictors in small data regimes and in the presence of measurement noise without overfitting to the data [32]. Further, Bayesian methods lend themselves to online model updating and could quickly improve the model’s predictive ability when introduced to new operating regions. Yet, there are disadvantages with probabilistic modeling and Bayesian inference. Except in special cases, inferring the posterior probability distribution of the model consists of solving intractable integrals and inference is slow for large datasets [33]. However, methods for approximation of the posterior distribution exist such as Markov Chain Monte Carlo (MCMC) sampling and variational inference (VI). Comparing these two approximation methods, VI has shown to scale better to large datasets and inference tends to be faster. Additionally, it simplifies posterior updating in the presence of new data. Nevertheless, the approximation with VI is in most cases bounded away from the true distribution, whereas MCMC methods will in principle converge towards the true distribution [33]. A challenge for data-driven probabilistic models, such as Bayesian neural networks, is that the model parameters are generally non-physical, and setting the parameter priors is nontrivial. Despite neural networks being among the more popular data-driven methods for VFM modeling, to the extent of the authors’ knowledge, there has been no attempt at using BNNs for VFM. There are, however,

examples of BNNs being used for data-driven prediction in similar applications [34, 35].

### 3. Flow rate measurements and dataset

A petroleum production well is illustrated in Figure 1. Produced fluids flow from the reservoir, up to the wellhead, and through the choke valve. The choke valve opening ( $u$ ) is operated to control the production from the well. The fluids thereafter enter the separator which separates the multiphase flow into the three single phases of oil, gas and water;  $\mathbf{q} = (q_{oil}, q_{gas}, q_{wat})$ . On well-instrumented wells, pressure ( $p$ ) and temperature ( $T$ ) is measured upstream and downstream the choke valve.

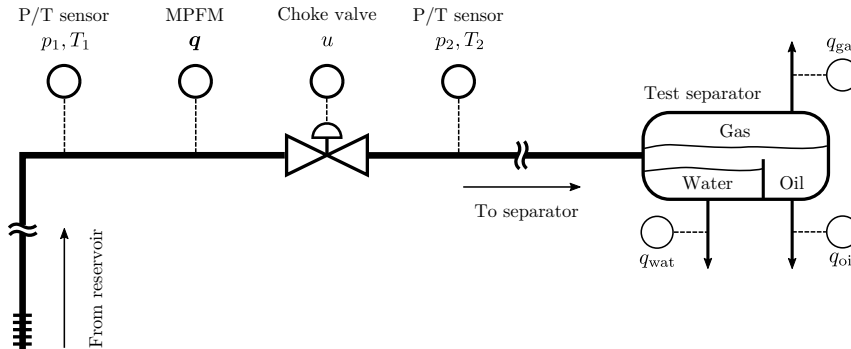


Figure 1: Sensor placement in a typical production well. A MPFM measures multiphase flow rates in the well. During well testing, single phase flow rates are measured with high accuracy after fluid separation.

There are two main ways to measure the multiphase flow rate through the well, multiphase flow meters (MPFMs), or well-testing, both illustrated in Fig. 1. MPFMs are complex devices based on several measurement principles and offer continuous measurements of the multiphase flow rate. Unfortunately, MPFMs have limited operation range, struggle with complex flow patterns, and are subject to drift over time [36]. Additionally, PVT (pressure-volume-temperature) data are used as part of the MPFM calculations and should be accurate and up-to-date for high accuracy MPFM measurements. On the other hand, a well test is an experiment where the multiphase flow rate is routed to a test separator whereby the separated flows is measured using single-phase measurement devices over a period of time (typically a few hours). Compared to the MPFM, well tests are performed infrequently, usually 1-2 times a month [2].

Normally, measurements of the multiphase flow rate obtained through well-testing have higher accuracy than the measurements from the MPFMs. This is due to the use of single-phase measurement devices in well-testing. According to [36, 37], the uncertainty, in terms of mean absolute percentage error, of

well tests, may potentially be as low as 2% and 1% for gas and oil respectively, whereas MPFM uncertainty is often reported to be around 10%. The error statistics are calculated with respect to reference measurements. For measurements of pressure, temperature, and choke openings, we assume that the sensors’ accuracy is high, typically with an uncertainty of 1% or less, and measurement error in these measurements are therefore neglected.

The flow rates are often given as volumetric flow rates under standard conditions, e.g. as standard cubic meter per hour ( $Sm^3/h$ ). Standard conditions make it easier to compare to reference measurements or measurements at other locations in the process as the volume of the fluid changes with pressure and temperature. Flow rates may be converted from actual conditions to standard conditions using PVT data [38]. If the density of the fluid at standard conditions is known, the standard volumetric flow rate may be converted to mass flow rate, and the phasic mass fractions,  $\boldsymbol{\eta} = (\eta_{oil}, \eta_{gas}, \eta_{wat})$ , may be calculated. We assume steady-state production, frozen flow, and incompressible liquid such that the phasic volumetric flow rate and mass fractions are constant through the system, from the reservoir to the separator.

### 3.1. Dataset

The dataset used in this study consists of 66 367 experiments from 60 wells producing from five oil and gas fields. For each well we have a sequence of experiments in time; the time span from the first to last experiment is plotted for each well in Figure 2a. The figure shows that the experiment frequency varies from a handful to hundreds of experiments per year. Each experiment consists of a measured total volumetric flow rate, *either* from a test separator *or* a MPFM (not both), and the measurements of the following explanatory variables: pressures and temperatures upstream and downstream the choke valve, choke opening, and mass fractions of oil and gas. In this study, 14 wells are tested with a test separator for which the average number of experiments is 163, whereas there are 46 wells tested with a MPFM and the average number of experiments is 1393. The 60 wells are quite different from each other in terms of produced fluids. Figure 2b illustrate the mass fractions represented in all experiments across all wells.

No experimental set-up was used to affect the data variety in these experiments; for example, we did not consider step well tests as in [14].

We preprocess the experiment data using a data squashing technology [39] to avoid short-scale instabilities. After preprocessing, each example represents an experiment performed during steady-state operation, which is suitable for modeling steady-state production rates. For each well, we collect the corresponding examples in a dataset  $\mathcal{D} = \{(\mathbf{x}_i, y_i)\}_{i=1}^N$  (in the following we will only consider one well at the time and simply refer to the dataset as  $\mathcal{D}$ ). The explanatory variables are  $\mathbf{x}_i = (u_i, p_{1,i}, p_{2,i}, T_{1,i}, T_{2,i}, \eta_{oil,i}, \eta_{gas,i})$ . The target variable  $y_i = q_{oil,i} + q_{gas,i} + q_{wat,i} \in \mathbb{R}$  is the total volumetric multiphase flow rate through the choke valve.

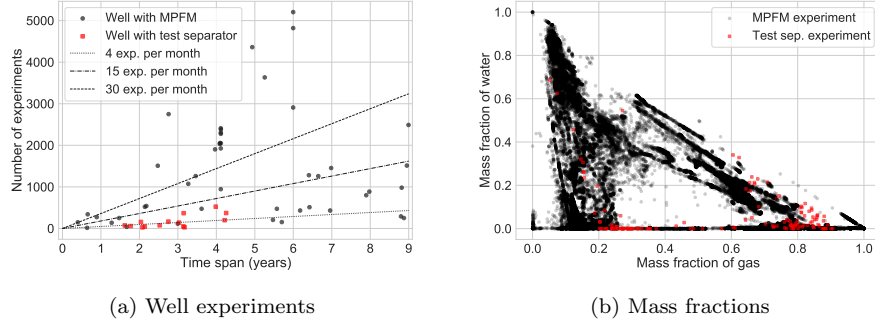


Figure 2: The number of well experiments is plotted against the time span from the first to last experiment in (a). The gas and water mass fraction for all experiments is shown in (b).

#### 4. Probabilistic flow model

We consider the following probabilistic model for the total multiphase flow rate:

$$\begin{aligned}
 y_i &= z_i + \epsilon_i, & \text{for } i = 1, \dots, N, \\
 z_i &= f(\mathbf{x}_i, \boldsymbol{\phi}), & \text{for } i = 1, \dots, N, \\
 s_i &= g(z_i, \boldsymbol{\psi}), & \text{for } i = 1, \dots, N, \\
 \epsilon_i &\sim \mathcal{N}(0, s_i^2), & \text{for } i = 1, \dots, N, \\
 \phi_i &\sim \mathcal{N}(a_i, b_i^2), & \text{for } i = 1, \dots, K_\phi, \\
 \psi_i &\sim \mathcal{N}(c_i, d_i^2), & \text{for } i = 1, \dots, K_\psi,
 \end{aligned} \tag{1}$$

where  $y_i$  is a measurement of the true, but unobserved multiphase flow rate  $z_i$  subject to additive measurement noise  $\epsilon_i$ . We assume  $z_i$  to depend nonlinearly on  $\mathbf{x}_i$ . We approximate the nonlinearity by a feed-forward neural network  $f(\mathbf{x}_i, \boldsymbol{\phi})$  with weights and biases represented by latent (random) variables  $\boldsymbol{\phi}$ . We assume the noise to be normally distributed with standard deviation  $g(z_i, \boldsymbol{\psi}) > 0$ , and we consider different functions  $g$  of  $z_i$  and latent variables  $\boldsymbol{\psi}$ . We discuss the priors on the latent variables,  $p(\boldsymbol{\phi})$  and  $p(\boldsymbol{\psi})$ , in the subsequent sections. The probabilistic model is illustrated graphically in Figure 3.

Given  $\boldsymbol{\phi}$ ,  $\boldsymbol{\psi}$  and explanatory variables  $\mathbf{x}$ , the conditional flow rate  $z = f(\mathbf{x}, \boldsymbol{\phi})$  and a measurement  $y$  is generated as

$$y | z, \boldsymbol{\psi} \sim \mathcal{N}(y | z, g(z, \boldsymbol{\psi})^2). \tag{2}$$

The flow rate measurement  $y$  is subject to epistemic (model) uncertainty in  $f(\mathbf{x}, \boldsymbol{\phi})$  and aleatoric (measurement) uncertainty via  $g(z, \boldsymbol{\psi})$ . We differ between homoscedastic and heteroscedastic measurement noise. Heteroscedasticity is when the structure of the noise in a signal is dependent on the structure of the signal itself and is more difficult to capture [40]. Homoscedasticity is the lack of heteroscedasticity.

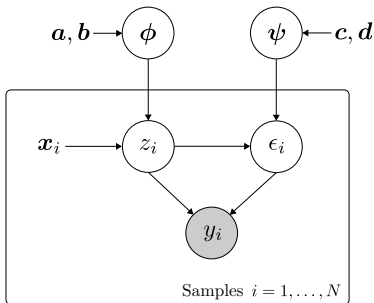


Figure 3: A probabilistic graphical model for flow rates. Random variables are inscribed by a circle. A gray-filled circle means that the random variable is observed. The dependence  $z_i \rightarrow \epsilon_i$  indicates that the noise is heteroscedastic, while the dependence  $\psi \rightarrow \epsilon_i$  indicates that the noise model is learned from data.

The flow model in (1) is a quite generic regression model, but restricts the modeling of the measurement noise. The model allows the noise to be heteroscedastic, with the noise level being a function of the flow rate  $z$ , or homoscedastic for which the noise level is fixed. In the latter case, we simply set  $g(z, \boldsymbol{\psi}) = \sigma_n$ , where  $\sigma_n$  is a fixed noise level. If the noise level is unknown, we can learn it with the following homoscedastic noise model:

$$\begin{aligned} g(z_i, \boldsymbol{\psi}) &= \exp(\psi_1), \\ \psi_1 &\sim \mathcal{N}(c_1, d_1^2), \end{aligned} \tag{3}$$

where  $\psi_1$  is a normally distributed latent variable and the noise level is log-normal. The exponential ensures that  $g(z_i, \boldsymbol{\psi}) > 0$ .

The homoscedastic noise model in (3) may be unrealistic for flow meters with a heteroscedastic noise profile. As described earlier, the uncertainty of the flow rate measurement is often given in relative terms. To model this property of the data, we augment (3) with a multiplicative term to get the following heteroscedastic noise model:

$$\begin{aligned} g(z_i, \boldsymbol{\psi}) &= \exp(\psi_2) \cdot |z_i| + \exp(\psi_1), \\ \psi_1 &\sim \mathcal{N}(c_1, d_1^2), \\ \psi_2 &\sim \mathcal{N}(c_2, d_2^2), \end{aligned} \tag{4}$$

where  $\psi_1$  and  $\psi_2$  are normally distributed latent variables<sup>1</sup>. Both  $\exp(\psi_1)$  and  $\exp(\psi_2)$  are log-normal, and are hence strictly positive. It follows from  $|z| \geq 0$  that the noise standard deviation  $g(z, \boldsymbol{\psi}) > 0$ .

<sup>1</sup>We assume that we have one flow rate instrument for each well. Yet, several instruments may be handled by having separate noise models for each instrument.

#### 4.1. Prior for the noise model, $p(\boldsymbol{\psi})$

The prior for the noise model is assumed to be a factorized normal

$$p(\boldsymbol{\psi}) = \prod_{i=1}^{K_\psi} \mathcal{N}(\psi_i | c_i, d_i^2), \quad (5)$$

where  $K_\psi = 1$  for the homoscedastic noise model in (3) and  $K_\psi = 2$  heteroscedastic noise model in (4).

The accuracy of an instrument measuring flow rate is commonly given as a mean absolute percentage error (MAPE) to a reference measurement. More precisely, the expected measurement error is specified as

$$\mathbf{E}_{y|z} \left[ \frac{|y - z|}{|z|} \right] = E_r, \quad (6)$$

where  $y$  is the measurement,  $z > 0$  is the reference measurement, and  $E_r$  is the MAPE; e.g.  $E_r = 0.1$  for a MAPE of 10%. We wish to translate such statements to a prior,  $p(\boldsymbol{\psi})$ .

Assuming a perfect reference measurement  $z$ , normal noise  $\epsilon$ , and an additive noise model  $y = z + \epsilon$ , we obtain from (6) a noise standard deviation  $g(z) = \sqrt{\pi/2} E_r |z|$ . We recognize this as the first term in the heteroscedastic noise model (4). We derive prior parameters of  $\psi_2 \sim \mathcal{N}(c_2, d_2^2)$  that correspond to a log-normal distribution  $\exp(\psi_2)$  with mean  $\sqrt{\pi/2} E_r$  by solving:

$$c_2 = \log(\sqrt{\pi/2} E_r) - d_2^2/2, \quad (7)$$

where we can adjust the variance  $d_2^2$  to express our uncertainty in the value of  $E_r$ .

The specification of a relative measurement error  $E_r$  cannot be translated directly to a fixed noise level, as required by the homoscedastic noise model in (3). However, we can obtain a reasonable approximation by using the above procedure. If we set  $z = \bar{z}$ , where  $\bar{z}$  is the mean production of a well, we can calculate prior parameters for  $\psi_1$  as follows:

$$c_1 = \log(\sqrt{\pi/2} E_r \bar{z}) - d_1^2/2. \quad (8)$$

We express our uncertainty about the noise level by adjusting the variance  $d_1^2$ .

#### 4.2. Prior for the neural network weights, $p(\boldsymbol{\phi})$

We encode our initial belief of the parameters  $\boldsymbol{\phi}$  with a fully factorized normal prior

$$p(\boldsymbol{\phi}) = \prod_{i=1}^{K_\phi} \mathcal{N}(\phi_i | a_i, b_i^2), \quad (9)$$

where  $K_\phi$  is the number of weights and biases in the neural networks  $f$ . We assume a zero mean for the weights and biases, that is  $a_i = 0$ , as is common

practice for neural networks. One interpretation of the prior standard deviations is that they encode the (believed) frequencies of the underlying function, with low values of  $\mathbf{b}$  inducing slow-varying (low frequency) functions, and high values inducing fast-varying (high frequency) functions [12]. While this interpretation can give us some intuition about the effect of the prior, it is not sufficiently developed to guide the specification of a reasonable prior. We refrain from learning the prior from the data (as with empirical Bayes) and therefore treat  $\mathbf{b}$  as hyperparameters to be prespecified.

For deep neural networks it is common practice to randomly sample the initial weights so that the output has a variance of one for a standard normal distributed input [41, 42]. For example, He-initialization [42] is often used for neural networks with ReLU activation functions. With He-initialization, the weights of layer  $l$  are drawn from the distribution  $\mathcal{N}(0, \sigma_l^2)$  with  $\sigma_l = \sqrt{2/n_l}$ , where  $n_l$  is the number of layer inputs. The weights in the first hidden layer are initialized with  $\sigma_l = \sqrt{1/n_l}$  since no ReLU activation is applied to the network’s input. With layer biases set to zero, this initialization scheme yields a unit variance for the output.

The objective of weight initialization is similar to that of prior specification; a goal in both settings is to find a good initial model. In this work, we use the standard deviations  $b_i = \sigma_l$  as a starting point for the prior specification (for weight  $i$  in layer  $l$  of a ReLU network). We call this the *He-prior*. The resulting standard deviations can then be increased (or decreased) if one believes that the underlying function amplifies (or diminishes) the input signal.

Figure 4 shows the effect of  $\mathbf{b}$  on the predictive uncertainty of a Bayesian neural network. With a common prior standard deviation (same for all weights), the output variance is sensitive to the network size (depth and width). This sensitivity complicates the prior specification, as illustrated for different network depths in the figure. The He-prior retains a unit output variance for different network sizes.

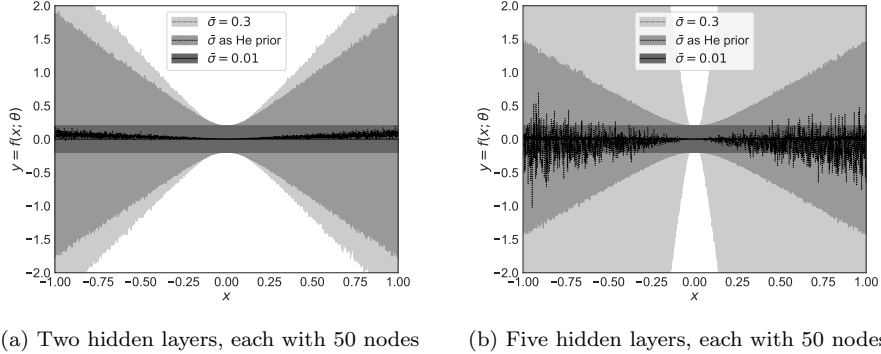


Figure 4: Prediction uncertainty (two sigma) for different priors  $b_i = \bar{\sigma}$  on a neural network's weights. Two networks are trained on a dataset  $\mathcal{D} = \{(0, y_i)\}_{i=1}^{100}$ , where  $y_i \sim \mathcal{N}(0, \sigma_n^2)$  and the noise level  $\sigma_n = 0.1$  is known. The figure shows that the epistemic (model) uncertainty is explained away for  $x = 0$  and increasing with the distance to  $x = 0$ . Away from the data, the increase in epistemic uncertainty depends on the prior variance and network depth.

#### 4.3. A fully factorized normal prior on the latent variables

The prior of model (1) is a fully factorized normal distribution,  $p(\phi)p(\psi)$ . To simplify the notation in the rest of this paper we collect the latent variables in  $\theta = (\phi, \psi) \in \mathbb{R}^K$ , where  $K = K_\phi + K_\psi$ . This allows us to state the prior on  $\theta$  as

$$p(\phi)p(\psi) = p(\theta) = \prod_{i=1}^K \mathcal{N}(\theta_i | \bar{\mu}_i, \bar{\sigma}_i^2), \quad (10)$$

with means  $\bar{\mu} = (\bar{\mu}_1, \dots, \bar{\mu}_K) = (a_1, \dots, a_{K_\phi}, c_1, \dots, c_{K_\psi}) \in \mathbb{R}^K$  and standard deviations  $\bar{\sigma} = (\bar{\sigma}_1, \dots, \bar{\sigma}_K) = (b_1, \dots, b_{K_\phi}, d_1, \dots, d_{K_\psi}) \in \mathbb{R}^K$ . The total number of model parameters ( $\bar{\mu}$  and  $\bar{\sigma}$ ) is  $2K$ .

## 5. Methods

We wish to infer the latent variables  $\theta$  of the flow rate model in (1) from observed data. With Bayesian inference, the initial belief of  $\theta$ , captured by the prior distribution  $p(\theta)$  in (10), is updated to a posterior distribution  $p(\theta | \mathcal{D})$  after observing data  $\mathcal{D}$ . The update is performed according to Bayes' rule:

$$p(\theta | \mathcal{D}) = \frac{p(\mathcal{D} | \theta)p(\theta)}{p(\mathcal{D})}, \quad (11)$$

where  $p(\mathcal{D})$  is the *evidence* and the *likelihood* is given by

$$p(\mathcal{D} | \theta) = \prod_{i=1}^N p(y_i | \mathbf{x}_i, \theta). \quad (12)$$

The log-likelihood of the model in (1) is shown in Appendix Appendix A.1.

From the posterior distribution, we can form the *predictive posterior distribution*

$$p(y^+ | \mathbf{x}^+, \mathcal{D}) = \int p(y^+ | \mathbf{x}^+, \boldsymbol{\theta}) p(\boldsymbol{\theta} | \mathcal{D}) d\boldsymbol{\theta} \quad (13)$$

to make a prediction  $y^+$  for a new data point  $\mathbf{x}^+$ .

The posterior in (11) involves intractable integrals that prevents a direct application of Bayes' rule [33]. In the following sections, we review two methods that circumvent this issue, namely maximum a posteriori (MAP) estimation and variational inference. With MAP estimation inference is simplified by considering only the mode of  $p(\boldsymbol{\theta} | \mathcal{D})$ , and with variational inference the posterior distribution is approximated. In the latter case, we can form an approximated predictive posterior distribution by replacing the posterior in (13) with its approximation. Statistics of this distribution, such as the mean and variance, can be estimated using Monte-Carlo sampling [12].

### 5.1. MAP estimation

With maximum a posteriori (MAP) estimation we attempt to compute:

$$\hat{\boldsymbol{\theta}}_{\text{MAP}} = \arg \max_{\boldsymbol{\theta}} p(\boldsymbol{\theta} | \mathcal{D}), \quad (14)$$

where  $\hat{\boldsymbol{\theta}}_{\text{MAP}}$  is the mode of the posterior distribution in (11). For the model in (1) with a fixed and constant noise variance  $\sigma_n^2$  and  $\bar{\sigma}_i^2$  is the (prior) variance of  $\theta_i$ , we have that

$$\begin{aligned} \hat{\boldsymbol{\theta}}_{\text{MAP}} &= \arg \max_{\boldsymbol{\theta}} \log p(\mathcal{D} | \boldsymbol{\theta}) + \log p(\boldsymbol{\theta}) \\ &= \arg \min_{\boldsymbol{\theta}} \frac{1}{2\sigma_n^2} \sum_{i=1}^N (y_i - f(\mathbf{x}_i, \boldsymbol{\theta}))^2 + \sum_{i=1}^K \frac{1}{2\bar{\sigma}_i^2} \theta_i^2, \end{aligned} \quad (15)$$

From (15), we see that MAP estimation is equivalent to maximum likelihood estimation with  $L^2$ -regularization [26].

While MAP estimation allows us to incorporate prior information about the model, it provides only a point estimate  $\hat{\boldsymbol{\theta}}_{\text{MAP}}$  and will not capture the epistemic uncertainty of the model. To obtain a posterior distribution of  $\boldsymbol{\theta}$  we consider the method of variational inference.

### 5.2. Variational inference

With variational inference, the posterior in (11) is approximated by solving an optimization problem; cf. [33]. Consider a variational posterior density  $q(\boldsymbol{\theta} | \boldsymbol{\lambda})$ , parameterized by a real vector  $\boldsymbol{\lambda}$ . The objective of the optimization is to find a density  $q^* = q(\boldsymbol{\theta} | \boldsymbol{\lambda}^*)$  that minimizes the Kullback-Leibler (KL) divergence to the exact posterior, i.e.

$$\boldsymbol{\lambda}^* = \arg \min_{\boldsymbol{\lambda}} D_{\text{KL}}(q(\boldsymbol{\theta} | \boldsymbol{\lambda}) \| p(\boldsymbol{\theta} | \mathcal{D})). \quad (16)$$

A direct approach to solve (16) is not practical since it includes the intractable posterior. In practice, the KL divergence is instead minimized indirectly by maximizing the *evidence lower bound* (ELBO):

$$\mathcal{L}(\boldsymbol{\lambda}) := \log p(\mathcal{D}) - D_{\text{KL}}(q(\boldsymbol{\theta} | \boldsymbol{\lambda}) \| p(\boldsymbol{\theta} | \mathcal{D})) \quad (17)$$

$$= \mathbf{E}_q[\log p(\mathcal{D} | \boldsymbol{\theta})] - D_{\text{KL}}(q(\boldsymbol{\theta} | \boldsymbol{\lambda}) \| p(\boldsymbol{\theta})), \quad (18)$$

where the expectation  $\mathbf{E}_q[\cdot]$  is taken wrt.  $q(\boldsymbol{\theta} | \boldsymbol{\lambda})$ . From the ELBO loss in (18), we see that an optimal variational distribution maximizes the expected log-likelihood on the dataset, while obtaining similarity to the prior via the regularizing term  $D_{\text{KL}}(q(\boldsymbol{\theta} | \boldsymbol{\lambda}) \| p(\boldsymbol{\theta}))$ .

### 5.2.1. Stochastic gradient variational Bayes

*Stochastic gradient variational Bayes* (SGVB) or *Bayes by backprop* is an efficient method for gradient-based optimization of the ELBO loss in (18); cf. [43, 44].

Suppose that the variational posterior  $q(\boldsymbol{\theta} | \boldsymbol{\lambda})$  is a *mean-field* (diagonal) normal distribution with mean  $\boldsymbol{\mu}$  and standard deviation  $\boldsymbol{\sigma}$ . Let the variational parameters be  $\boldsymbol{\lambda} = (\boldsymbol{\mu}, \boldsymbol{\rho})$  and compute  $\boldsymbol{\sigma} = \log(1 + \exp(\boldsymbol{\rho}))$ , where we use an elementwise softplus mapping to ensure that  $\sigma_i > 0$ .

The basic idea of SGVB is to *reparameterize* the latent variables to  $\boldsymbol{\theta} = h(\boldsymbol{\zeta}, \boldsymbol{\lambda}) = \boldsymbol{\mu} + \log(1 + \exp(\boldsymbol{\rho})) \circ \boldsymbol{\zeta}$ , where  $\circ$  denotes pointwise multiplication and  $\boldsymbol{\zeta} \sim \mathcal{N}(0, I)$ . With this formulation, the stochasticity of  $\boldsymbol{\theta}$  is described by a standard normal noise  $\boldsymbol{\zeta}$  which is shifted by  $\boldsymbol{\mu}$  and scaled by  $\boldsymbol{\sigma}$ . The reparameterization allows us to compute the gradient of the ELBO (18) as follows:

$$\begin{aligned} \nabla_{\boldsymbol{\lambda}} \mathcal{L}(\boldsymbol{\lambda}) &= \nabla_{\boldsymbol{\lambda}} \mathbf{E}_q[\log p(\mathcal{D} | \boldsymbol{\theta})] - \nabla_{\boldsymbol{\lambda}} D_{\text{KL}}(q(\boldsymbol{\theta} | \boldsymbol{\lambda}) \| p(\boldsymbol{\theta})) \\ &= \mathbf{E}_{\boldsymbol{\zeta}}[\nabla_{\boldsymbol{\theta}} \log p(\mathcal{D} | \boldsymbol{\theta}) \nabla_{\boldsymbol{\lambda}} h(\boldsymbol{\zeta}, \boldsymbol{\lambda})] - \nabla_{\boldsymbol{\lambda}} D_{\text{KL}}(q(\boldsymbol{\theta} | \boldsymbol{\lambda}) \| p(\boldsymbol{\theta})) \end{aligned} \quad (19)$$

The expectation in (19) can be approximated by Monte-Carlo sampling the noise:  $\boldsymbol{\zeta}_i \sim \mathcal{N}(0, I)$  for  $i = 1, \dots, M$ . If we also approximate the likelihood by considering a mini-batch  $\mathcal{B} \subset \mathcal{D}$  of size  $B \leq N$ , we obtain the unbiased SGVB estimator of the ELBO gradient:

$$\begin{aligned} \nabla_{\boldsymbol{\lambda}} \mathcal{L}(\boldsymbol{\lambda}) \simeq \nabla_{\boldsymbol{\lambda}} \hat{\mathcal{L}}(\boldsymbol{\lambda}) &:= \frac{N}{B} \frac{1}{M} \sum_{i=1}^M \nabla_{\boldsymbol{\theta}} \log p(\mathcal{B} | \boldsymbol{\theta}) \nabla_{\boldsymbol{\lambda}} h(\boldsymbol{\zeta}_i, \boldsymbol{\lambda}) \\ &\quad - \nabla_{\boldsymbol{\lambda}} D_{\text{KL}}(q(\boldsymbol{\theta} | \boldsymbol{\lambda}) \| p(\boldsymbol{\theta})). \end{aligned} \quad (20)$$

An advantage with the SGVB estimator in (20) is that we can utilize the gradient of the model  $\nabla_{\boldsymbol{\theta}} \log p(\mathcal{B} | \boldsymbol{\theta})$  as computed by back-propagation. When both the variational posterior and prior are mean-field normals, as is the case for our model,  $D_{\text{KL}}(q(\boldsymbol{\theta} | \boldsymbol{\lambda}) \| p(\boldsymbol{\theta}))$  can be computed analytically as shown in Appendix Appendix A.2.

In Algorithm 1 we summarize the basic SGVB algorithm for mean-field normals and Monte-Carlo sample size of  $M = 1$ . We finally note that for variables

representing weights of a neural network, we implement the *local reparameterization trick* in [45] to reduce gradient variance and save computations (not shown in Algorithm 1).

---

**Algorithm 1** Basic implementation of SGVB for mean-field normals ( $M = 1$ )

---

**Require:** data  $\mathcal{D}$ , model  $p(\mathcal{D}, \boldsymbol{\theta}) = p(\mathcal{D} | \boldsymbol{\theta})p(\boldsymbol{\theta})$ , parameters  $\boldsymbol{\lambda} = (\boldsymbol{\mu}, \boldsymbol{\rho})$ , learning rate  $\alpha$ .

- 1: **repeat**
  - 2:   Sample mini-batch  $\mathcal{B}$  from  $\mathcal{D}$
  - 3:   Sample  $\boldsymbol{\zeta} \sim \mathcal{N}(0, I)$
  - 4:    $\boldsymbol{\theta} \leftarrow \boldsymbol{\mu} + \log(1 + \exp(\boldsymbol{\rho})) \circ \boldsymbol{\zeta}$
  - 5:   Compute  $\nabla_{\boldsymbol{\lambda}} \hat{\mathcal{L}}(\boldsymbol{\lambda})$  using (20)
  - 6:    $\boldsymbol{\lambda} \leftarrow \boldsymbol{\lambda} + \alpha \nabla_{\boldsymbol{\lambda}} \hat{\mathcal{L}}(\boldsymbol{\lambda})$
  - 7: **until** no improvement in ELBO
  - 8: **return**  $\boldsymbol{\lambda}$
- 

## 6. Case study

The goal of our case study was to investigate the predictive performance and generalization ability of the proposed VFM. We implemented the probabilistic flow rate model in Section 4 and developed models using the dataset described in Section 3.1. The conditional mean flow rate,  $f(\boldsymbol{x} | \boldsymbol{\phi})$ , was modeled using feed-forward neural networks. Three different noise models were considered: a homoscedastic model with fixed noise standard deviation  $g(z | \boldsymbol{\psi}) = \sigma_n = \text{const.}$ ; a homoscedastic model with learned noise standard deviation, (3); and a heteroscedastic model with learned noise standard deviation, (4). For each of the three model types and the 60 wells in the dataset, we trained a neural network using the SGVB method in Section 5.2.1. We refer to these models by the label VI-NN. For comparison, we also trained a neural network for each of the wells using the MAP estimation method in Section 5.1. For these models we considered the measurement noise to be homoscedastic with a fixed noise standard deviation ( $\sigma_n$ ). We label these models as MAP-NN. The He-prior was used for the hidden layers to initialize and regularize the parameters; see Section 4.2. For the noise models, we set the priors as described in Section 4.1, differentiating between wells with MPFM and test separator experiments. The network architecture was fixed to three hidden layers, each with 50 nodes to which we apply the ReLU activation function [46]. Using practical recommendations in [47], the network architecture may be large as long as regularization is used to prevent overfitting. The Adam optimizer [48] was used to train all networks and we used early stopping with a validation dataset to avoid overfitting [49].

The case study is structured as follows. Firstly, we investigate the predictive performance of the four model types (three VI-NNs and MAP-NN) on each well for both historical and future data. If the models generalize well, we should expect a similar accuracy across all wells for each model type on both historical

and future data. Secondly, an important aspect of the VI-NNs is the ability to quantify the prediction uncertainty. We study the accuracy of the prediction uncertainty by looking at the calibration of the VI-NNs. Lastly, we investigate the effect of training set size on the predictive performance on future data.

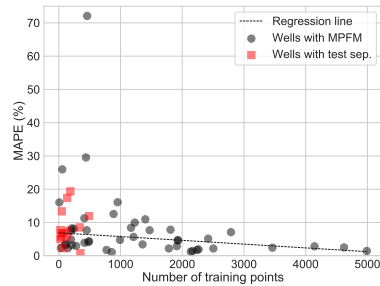
### 6.1. Prediction performance on historical data

To investigate the predictive performance on historical data, we set aside a three month long period of contiguous data, located in the middle of the dataset (when ordered chronologically), for testing. The rest of the data was used for model development. We randomly sampled 20% of the training data to be used for model validation. We analyze the performance for each model type, across the 60 wells. Table 1 shows the three error statistics: mean square error (MSE), mean absolute error (MAE), and mean absolute percentage error (MAPE) for the percentiles 25%, 50% (median) and 75%. Figure 5 show an overview of the spread in the MAPE for all well models as a function of the dataset size.

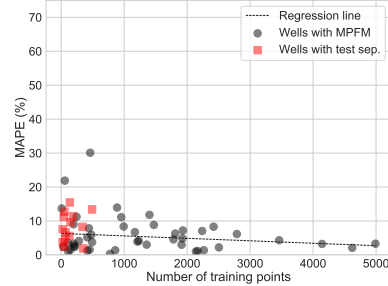
In general, we see that the prediction performance on historical data is adequate in which 25% of all well models have a MAPE of less than 4%. This is in line with some of the best reported results in literature, see Section 1. In fact, the best performing well model achieved an error of 0.3%. Yet, some well models obtain an unsatisfactory and very large error. The overall worst-performing model (MAP-NN) achieved an error of 72.1%.

Table 1: Prediction performance on historical test data. Reported values are the percentiles ( $p_{25}$ ,  $p_{50}$ ,  $p_{75}$ ) for each statistic.

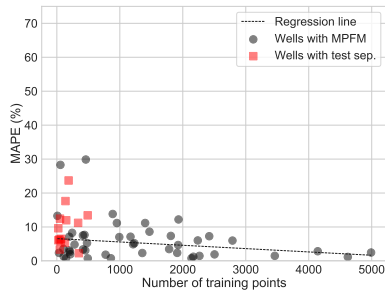
Well group	Method and model	MSE	MAE	MAPE %
All	MAP-NN fixed homosc.	0.4, 1.2, 2.9	0.5, 0.9, 1.3	2.8, 5.1, 8.3
	VI-NN fixed homosc.	0.2, 1.0, 4.3	0.4, 0.8, 2.4	2.6, 4.8, 8.5
	VI-NN learned homosc.	0.2, 1.0, 4.1	0.4, 0.8, 1.4	2.4, 5.3, 8.4
	VI-NN learned heterosc.	0.4, 1.5, 3.6	0.5, 1.0, 1.4	3.5, 5.9, 9.7
Test sep.	MAP-NN fixed homosc.	0.7, 2.2, 2.9	0.7, 1.1, 1.3	5.7, 7.2, 11.1
	VI-NN fixed homosc.	0.7, 2.7, 4.7	0.8, 1.1, 1.7	4.9, 7.9, 11.3
	VI-NN learned homosc.	1.2, 3.0, 4.5	0.8, 1.3, 1.6	5.8, 8.1, 12.3
	VI-NN learned heterosc.	1.1, 3.0, 4.3	0.8, 1.1, 1.9	5.1, 9.5, 11.4
MPFM	MAP-NN fixed homosc.	0.4, 1.0, 2.5	0.4, 0.9, 1.3	2.4, 4.4, 8.1
	VI-NN fixed homosc.	0.2, 0.9, 3.5	0.4, 0.7, 1.3	2.3, 4.1, 7.7
	VI-NN learned homosc.	0.2, 0.5, 2.5	0.3, 0.6, 1.3	2.0, 4.1, 7.3
	VI-NN learned heterosc.	0.2, 1.4, 2.4	0.4, 1.0, 1.3	3.1, 5.1, 8.6



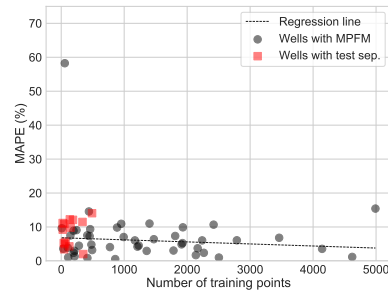
(a) MAP-NN with fixed homoscedastic noise



(b) VI-NN with fixed homoscedastic noise



(c) VI-NN with learned homoscedastic noise



(d) VI-NN with learned heteroscedastic noise

Figure 5: MAPE on historical test data plotted against the size of the training dataset. A robust linear regression line is fitted to the data.

## 6.2. Prediction performance on future data

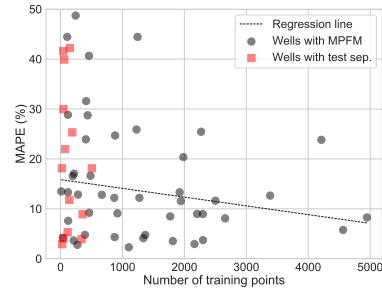
To analyze the predictive performance on future data, we set aside the last three months of experiments for testing. As before, the rest of the data was used in model development and 20% of that data was used for model validation. Table 2 shows the percentiles 25%, 50% and 75% of the MSE, MAE and MAPE of the different model types and well groups across all 60 well models. Figure 6 shows the MAPE against the number of data points for each well model.

Comparing to the results on historical data in Section 6.1, we see that the error is in general larger on prediction of future data. In particular, the MAPE of the 75% best-performing well models are in the range 16-24% on future data compared to 8-10% on historical data. Yet, the 25% best-performing models still achieve an MAPE of less than 6% with the overall best performing model obtaining an MAPE of 1.1%.

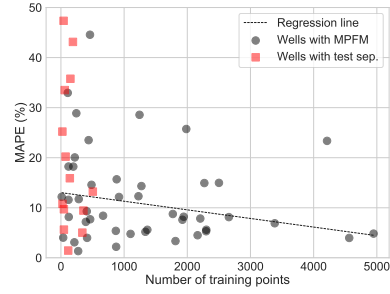
Looking at the performance of the different model types, we find that the VI-NN with learned heteroscedastic noise consistently outperforms the MAP-NN. The  $p_{75}$  MAPE across all wells is 24.1% for MAP-NN, compared to 15.7% for the heteroscedastic VI-NN, indicating that the VI-NN provides more robust predictions.

Table 2: Prediction performance on future test data. Reported values are the percentiles ( $p_{25}$ ,  $p_{50}$ ,  $p_{75}$ ) for each statistic.

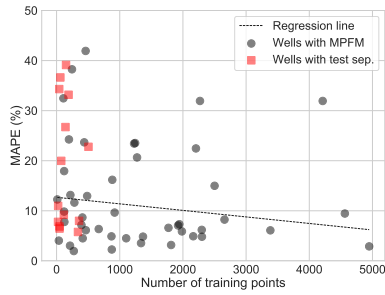
Well group	Method and model	MSE	MAE	MAPE %
All	MAP-NN fixed homosc.	1.3, 4.2, 15.8	0.9, 1.6, 3.2	5.6, 12.4, 24.1
	VI-NN fixed homosc.	1.3, 3.3, 12.0	0.9, 1.6, 2.4	5.6, 9.6, 18.2
	VI-NN learned homosc.	1.3, 3.6, 10.8	0.9, 1.5, 2.4	6.0, 8.9, 22.5
	VI-NN learned heterosc.	1.1, 2.9, 9.5	0.8, 1.4, 2.2	5.0, 9.2, 15.7
Test sep.	MAP-NN fixed homosc.	1.0, 2.7, 9.3	0.9, 1.3, 2.7	6.2, 18.1, 28.8
	VI-NN fixed homosc.	1.1, 4.6, 10.3	0.9, 1.8, 2.9	9.5, 14.6, 31.4
	VI-NN learned homosc.	1.7, 3.6, 13.4	1.0, 1.7, 3.1	7.8, 15.5, 31.6
	VI-NN learned heterosc.	1.3, 2.7, 5.5	0.9, 1.5, 2.0	6.0, 10.6, 18.6
MPFM	MAP-NN fixed homosc.	1.4, 5.8, 17.6	0.9, 1.6, 3.3	6.2, 12.2, 23.0
	VI-NN fixed homosc.	1.7, 3.2, 12.5	0.9, 1.4, 2.0	5.3, 8.3, 15.0
	VI-NN learned homosc.	1.3, 3.5, 9.9	0.8, 1.4, 2.3	4.9, 8.0, 17.5
	VI-NN learned heterosc.	1.1, 3.1, 10.7	0.8, 1.4, 2.3	4.7, 8.9, 14.9



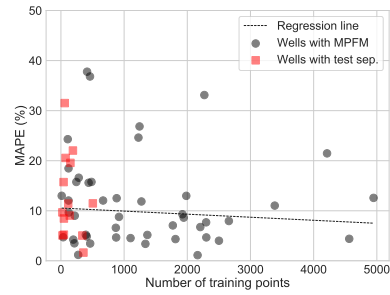
(a) MAP-NN with fixed homosc. noise



(b) VI-NN with fixed homosc. noise



(c) VI-NN with learned homosc. noise



(d) VI-NN with learned heterosc. noise

Figure 6: MAPE on future test data plotted against the size of the training dataset. A robust linear regression line is fitted to the data.

### 6.3. Uncertainty quantification and analysis

In contrary to the MAP-NN models, the VI-NN models quantify the uncertainty in their predictions. To study the quality of the prediction uncertainty, we generated a calibration plot for the three different noise models using the test dataset in each of the case studies in Section 6.1 and 6.2; see Figure 7. The plot shows the frequency of residuals lying within varying thresholds of the predicted distribution. For instance, for a perfectly calibrated model one should expect 20% of the test points to be in the  $p_{20}$  percentile of the predictive distribution. In other words, a perfectly calibrated model will lie on the diagonal gray line illustrated in the figures. In order to visualize the diversity of the different well calibrations, we have illustrated the 25% and 75% percentile at each probability threshold for all well models.

On historical data, the models trained on test separator measurements seem to be best calibrated. The models trained on MPFM measurements overestimate the uncertainty in their predictions. On future data, the results are reversed. The models trained on MPFM measurements are the better calibrated and the models trained on test separator measurements all underestimate the prediction uncertainty. Overall, the calibration improves when the noise model is learned; as seen clearly when comparing the fixed homoscedastic noise to the learned heteroscedastic noise model. The results are summarized in Table 3, which show the coverage probabilities (using the point-wise median in the calibration plots) at the 95% probability threshold.

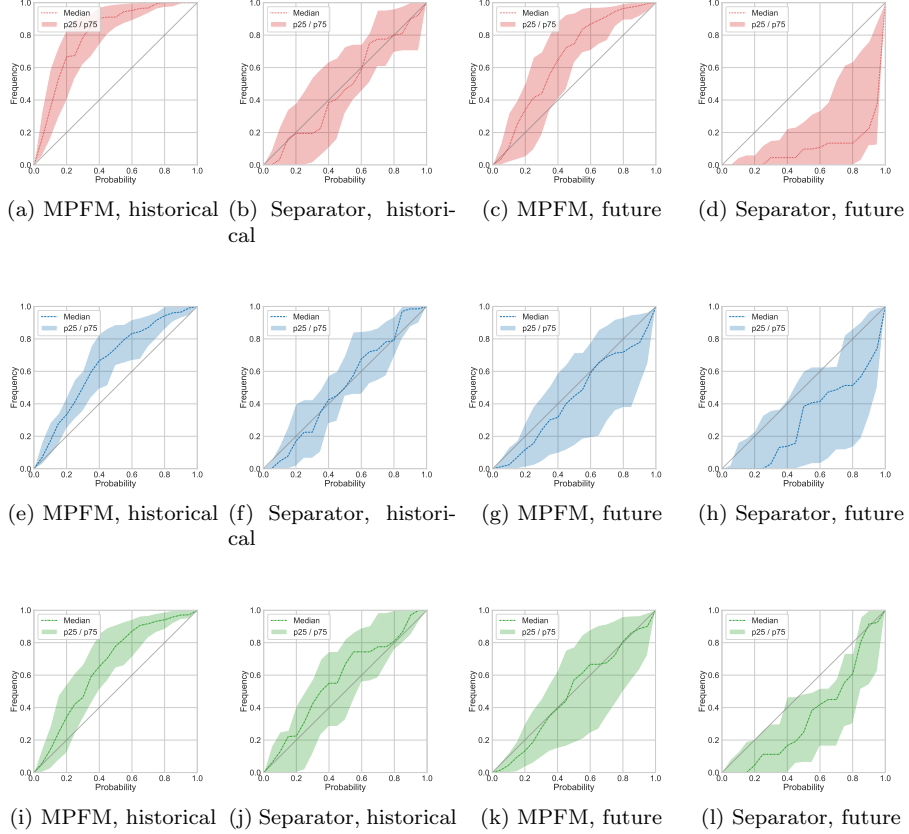


Figure 7: Calibration plots for fixed homoscedastic noise (a-d), learned homoscedastic noise (e-h), and learned heteroscedastic noise (i-l). Wells are grouped by measurement type, MPFM or test separator, and we show calibration on historical test data (Section 6.1) and future test data (Section 6.2). Shown is the median frequency (dashed line) at each probability threshold (x-axis). The  $(p_{25}, p_{75})$  percentiles (band) show the variation in calibration across wells. A perfectly calibrated model would lie on the diagonal line  $y = x$ .

Table 3: Coverage probability (95%)

Case	Method and model	Test sep. (%)	MPFM (%)
Future prediction	VI-NN fixed homosc.	37.5	99.5
	VI-NN learned homosc.	81.0	87.7
	VI-NN learned heterosc.	92.3	90.0
Historical prediction	VI-NN fixed homosc.	92.4	100.0
	VI-NN learned homosc.	98.5	99.1
	VI-NN learned heterosc.	100.0	97.2

#### 6.4. Effect of training set size on prediction performance

The results reported in the previous sections, Section 6.1 and 6.2 suggested that the prediction error tends to decrease as the training set size increases. Yet, previous studies such as [10], indicate that model performance does not necessarily improve when including data that is several years old. To closer inspect this effect, we compared models developed on successively larger training sets.

To allow for a interesting range of dataset sizes we considered a subset of 21 wells with 1200 or more MPFM experiments. In a number of trials, we randomly picked a well and a location at which to split the dataset into a training and test set. Keeping the test set fixed, we created a sequence of increasingly large training sets preceding the test data in time. We considered the following training set sizes: 150, 200, 300, ..., 1100; where we increment by 100 between 300 and 1100. We developed a MAP-NN model for each of these training sets, using early stopping and validating against the last 100 data points. The test set size was also set to 100 data points, spanning on average 90 days of production.

Denoting the test MAPE of the models by  $e_{150}$ ,  $e_{200}$ ,  $e_{300}$ , ...,  $e_{1100}$ , we computed *relative* MAPEs

$$r_k = \frac{e_k}{e_{150}}, \text{ for } k \in \{150, 200, 300, \dots, 1100\}. \quad (21)$$

The relative errors allowed us to measure how the errors developed as the training set size was increased, with a baseline at  $r_{150} = 1$ . The result of 65 trials is shown in Figure 8.

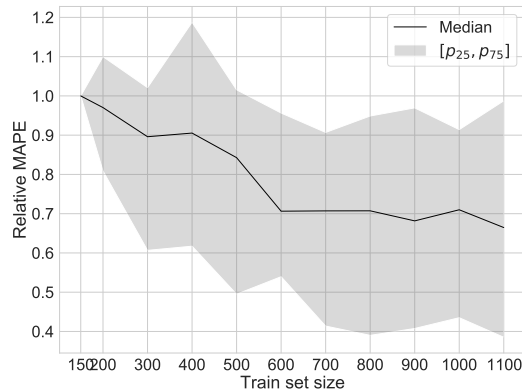


Figure 8: Relative test errors for increasing training set sizes.

## 7. Discussion

In Section 1.1 we discussed some of the challenges faced by data driven VFMs. These were: (1) small data regime; (2) poor measurement quality; and

(3) non-stationarity of the underlying process. Here we discuss the results in light of these challenges. All results are discussed in terms of MAPE values.

### 7.1. Performance on historical and future test data

First we discuss the concern about non-stationarity of the underlying process. This means the distribution of values seen during training is not necessarily the same as the distribution of values used for testing. The effect of this is best observed when comparing the performance on historical and future data; see Table 1 and 2. Looking at the upper and lower percentiles, we see the different models achieve a performance in the range of 2-11% error on historical data and 5-30% error on future data. Since the strength of data-driven models lies with interpolation, rather than extrapolation, it is natural that the performance is worse on the future data case. Compared to our target threshold on VFM performance of 10% MAPE, the performance is acceptable on historical data. On this case, at least 75% of the models achieve the target performance for all the model types considered. On the future data case the performance falls short of the target, and we obtain a MAPE of 9-13% or less for approximately half of the models. This indicates that the robustness of the methods is inadequate for use in a commercial VFM, according to our requirements in Section 1.2. For real time application, frequent model updates are likely required to achieve the performance seen on historical data. This raises the technical challenge of implementing a data-driven modeling approach.

The study on dataset size in Section 6.4 further explores the development of data distributions and the effect older data has on future prediction errors. The result, seen in Figure 8, indicates that additional data is only valuable up to a certain point, after which older data will no longer be useful when predicting future values. The point where this happens will naturally vary between wells. For the wells included here, this happens at 600 data points on average, for which the additional data is approximately 18 months or longer into the past. Looking at Figure 6, we again see the trend that wells with more data perform better, but only up to a certain point. We remark that insufficient model capacity would have a similar effect on the performance; however, we find this to be unlikely in our case due to the high capacity and low training errors of the neural networks used.

A second concern raised was related to small data regimes. The results mentioned above also illustrates the effect of small data. Looking at Figure 5 and Figure 6 we see a higher variance in performance among wells with less than 700 datapoints. This is concerning because many of the wells, in particular those with well test experiments as their primary source of data, have very few experiments. Based on the median MAPE values in Table 1 and 2, models trained on MPFM data outperforms the models trained on test separator data. This indicates that data quantity may outweigh data quality in the small-data regime.

The three different noise models perform similarly in terms of MAPE, on both historical and future data. The only exception being the learned heteroscedastic noise model, which performed better than the others on the future

data case when judged by the  $p_{75}$  values. This is believed to be because the heteroscedastic error term give the objective function some added robustness towards large errors.

The wells that lie in the top quarter of performance achieved MAPE values comparable to the earlier works discussed in Section 1. However, this performance seems difficult to achieve for the full set of wells. The difficulty in generalizing a single model architecture to a broad set of wells is troublesome for potential commercialization of ML-based VFM.

### 7.2. Noise models

The last concern raised was poor data quality. In particular uncertainty in flow rate measurements, and potential gross errors in MPFM measurements.

From the calibration plots in Figure 7, we see that learning the noise model improves the calibration. The calibration curves for models trained on MPFM data generally lie above the curves for models trained on test separator data, both for historical and future predictions. This means that models trained on MPFM measurements are less confident in their predictions, even though they are trained on more data. It was suspected that models trained on MPFM data would reflect the increased uncertainty present in these measurements, but this is difficult to observe from the results. It is worth noting that the MPFM models are tested on MPFM data, so any systematic errors present in the MPFM itself will not be detected.

Because the models have potentially large prediction errors (especially for future data), it is desirable that the model can assess its own performance. The coverage probabilities reported in Table 3 give us some confidence in the uncertainty estimates for the learned noise models, especially for the historical cases.

Neither the homoscedastic (3) or heteroscedastic (4) noise model can capture complex noise profiles that operate on the flow conditions,  $\mathbf{x}$ . As most flow meters are specialized to accurately measure flow rates for certain compositions and flow regimes, this is a potential drawback of the models. We leave it to later works to address such limitations, but note that with few adjustments the flow model in (1) can accommodate heteroscedasticity of a rather general form.

### 7.3. Bayesian neural networks

As stated in Section 1, setting the priors is not a trivial task and in several papers the Kullback-Leibler divergence term in the ELBO loss, Equation (18), is down-weighted to improve model performance due to poor priors. This remains a research question, however, in Section 4.2 we describe one way of approaching prior specification in BNNs. The difficulty of setting priors combined with small datasets, may make it difficult to successfully train models of this complexity. Still, the results are reasonable in the historical data case, and the estimated uncertainty is still better than only relying on point estimates.

## 8. Concluding remarks

One of the use cases for data-driven VFMs is to predict flow rates in real time, with low cost and minimal maintenance. Towards this end, the methods explored here are able to achieve acceptable performance (or better) on approximately half of the wells tested. This does not mean that the methods (MAP and VI) are flawed, but rather that the discussed data challenges limit the achievable performance. We consider the tested approach to modeling of flow rates from historical data, which is similar to other works, to yield models that lack robustness towards a changing environment.

Of the three initial data challenges, the non-stationary data distribution appears to be the most concerning. In practice, this will cause each well to be trapped in a small data regime as older data becomes irrelevant. It also means that we want models with decent extrapolating properties, which is inherently challenging for data-driven approaches. This data issue limits the performance of all the models we consider in this paper. We did, however, find VI to provide more robust predictions than MAP estimation on future data. In this case, we obtained the best performance with the heteroscedastic VI-NN, indicating that a heteroscedastic model can be advantageous for flow rate measurements.

The BNN approach is promising due to its ability to provide uncertainty estimates. However, we did not consistently obtain well-calibrated models for the wells explored here. We attribute this to the difficulty of setting meaningful priors for neural networks weights, and the fact that priors play a significant role in small data regimes. As a result, the uncertainty estimates provided by the BNNs should be used with caution.

The results indicate that it can be challenging to find a single model architecture with acceptable performance for a broad set of wells. Additionally, frequent model updates are likely required in order to keep a acceptable performance. This poses a technical challenge in terms of VFM maintenance.

We would suggest future research to focus on ways to overcome the challenges related to small data and non-stationary data distributions. Advances on these problems are likely required to improve the robustness and extrapolation capabilities of models used in real-time applications. We believe two promising avenues of research to be: hybrid data-driven, physics-based models that enable us to set stronger priors; and, data-driven architectures that allow us to incorporate a larger quantity of data into the training procedure, for instance by sharing parameters between well models.

## Acknowledgements

This work was supported by Solution Seeker AS.

## Appendix A. Derivations

### Appendix A.1. Log-likelihood of the flow rate model

The log-likelihood of the flow model in (1) with parameters  $\boldsymbol{\theta} = (\boldsymbol{\phi}, \boldsymbol{\psi})$  on a dataset  $\mathcal{D} = (X, \mathbf{y}) = \{(\mathbf{x}_i, y_i)\}_{i=1}^N$  is given by

$$\begin{aligned} \log p(\mathbf{y} | X, \boldsymbol{\theta}) &= \sum_{i=1}^N \log p(y_i | \mathbf{x}_i, \boldsymbol{\theta}) \\ &= \sum_{i=1}^N \log \mathcal{N}(y_i | f(\mathbf{x}_i, \boldsymbol{\phi}), g(f(\mathbf{x}_i, \boldsymbol{\phi}), \boldsymbol{\psi})^2) \\ &= -\frac{N}{2} \log(2\pi) - \sum_{i=1}^N \log g(f(\mathbf{x}_i, \boldsymbol{\phi}), \boldsymbol{\psi}) - \frac{1}{2} \left( \frac{y_i - f(\mathbf{x}_i, \boldsymbol{\phi})}{g(f(\mathbf{x}_i, \boldsymbol{\phi}), \boldsymbol{\psi})} \right)^2. \end{aligned} \quad (\text{A.1})$$

With a homoscedastic noise model  $g(z, \boldsymbol{\psi}) = \sigma_n = \text{const.}$ , the log-likelihood simplifies to:

$$\log p(\mathbf{y} | X, \boldsymbol{\theta}) = -\frac{N}{2} \log(2\pi\sigma_n^2) - \frac{1}{2\sigma_n^2} \sum_{i=1}^N (y_i - f(\mathbf{x}_i, \boldsymbol{\phi}))^2. \quad (\text{A.2})$$

### Appendix A.2. Kullback-Leibler divergence term, $D_{KL}(q(\boldsymbol{\theta} | \boldsymbol{\lambda}) \| p(\boldsymbol{\theta}))$

Let the approximation  $q(\boldsymbol{\theta} | \boldsymbol{\lambda})$  and prior  $p(\boldsymbol{\theta})$  be mean-field normal distributions of the random variables  $\boldsymbol{\theta} \in \mathbb{R}^K$ . Assume that the approximation is parameterized with  $\boldsymbol{\lambda} = (\boldsymbol{\mu}, \boldsymbol{\rho})$ , where  $\boldsymbol{\mu}$  is the mean and  $\boldsymbol{\sigma} = \log(1 + \exp(\boldsymbol{\rho}))$  is the standard deviation of  $q$ . Then, the Kullback-Leibler divergence is given as:

$$\begin{aligned} D_{KL}(q(\boldsymbol{\theta} | \boldsymbol{\lambda}) \| p(\boldsymbol{\theta})) &= \mathbf{E}_q [\log q(\boldsymbol{\theta} | \boldsymbol{\lambda}) - \log p(\boldsymbol{\theta})] \\ &= \mathbf{E}_q \left[ \sum_{i=1}^K \log q(\theta_i | \lambda_i) - \log p(\theta_i) \right] \\ &= \frac{1}{2} \mathbf{E}_q \left[ \sum_{i=1}^K -\log(2\pi\sigma_i^2) - \left( \frac{\theta_i - \mu_i}{\sigma_i} \right)^2 + \log(2\pi\bar{\sigma}_i^2) + \left( \frac{\theta_i - \bar{\mu}_i}{\bar{\sigma}_i} \right)^2 \right] \\ &= \frac{1}{2} \left[ \sum_{i=1}^K -2\log \frac{\sigma_i}{\bar{\sigma}_i} - \frac{1}{\sigma_i^2} \underbrace{\mathbf{E}_{q_i} [(\theta_i - \mu_i)^2]}_{=\sigma_i^2} + \frac{1}{\bar{\sigma}_i^2} \mathbf{E}_{q_i} [(\theta_i - \bar{\mu}_i)^2] \right] \quad (\text{A.3}) \\ &= \frac{1}{2} \sum_{i=1}^K \left[ -1 - 2\log \frac{\sigma_i}{\bar{\sigma}_i} + \frac{1}{\bar{\sigma}_i^2} \mathbf{E}_{q_i} [(\theta_i - \bar{\mu}_i)^2] \right] \\ &= \frac{1}{2} \sum_{i=1}^K \left[ -1 - 2\log \frac{\sigma_i}{\bar{\sigma}_i} + \left( \frac{\mu_i - \bar{\mu}_i}{\bar{\sigma}_i} \right)^2 + \left( \frac{\sigma_i}{\bar{\sigma}_i} \right)^2 \right] \end{aligned}$$

## References

- [1] J.-D. Jansen, *Nodal Analysis of Oil and Gas Wells - Theory and Numerical Implementation*, Delft University of Technology, TU Delft, The Netherlands, 2015.
- [2] D. D. Monteiro, M. M. Duque, G. S. Chaves, V. M. F. Filho, J. S. Baioco, Using data analytics to quantify the impact of production test uncertainty on oil flow rate forecast, *IFP Energies Nouvelles* 75 (2020).
- [3] E. Toskey, Improvements to Deepwater Subsea Measurements RPSEA Program: Evaluation of Flow Modeling, in: *Proceedings of the Annual Offshore Technology Conference*, 2012.
- [4] T. Bikmukhametov, J. Jäschke, First Principles and Machine Learning Virtual Flow Metering: A Literature Review, *Journal of Petroleum Science and Engineering* 184 (2020).
- [5] D. Solle, B. Hitzmann, C. Herwig, M. P. Remelhe, S. Ulonska, L. Wuerth, A. Prata, T. Steckenreiter, Between the poles of data-driven and mechanistic modeling for process operation, *Chemie Ingenieur Technik* (2016).
- [6] A. Amin, Evaluation of Commercially Available Virtual Flow Meters (VFMs), in: *Proceedings of the Annual Offshore Technology Conference*, 2015, pp. 1293–1318.
- [7] K. Balaji, M. Rabiei, V. Suicmez, C. H. Canbaz, Z. Agharzeyva, S. Tek, U. Bulut, C. Temizel, Status of data-driven methods and their application in oil and gas industry, in: *EAGE Conference and exhibition*, Society of Petroleum Engineers, 2018.
- [8] T. A. AL-Qutami, R. Ibrahim, I. Ismail, M. A. Ishak, Radial basis function network to predict gas flow rate in multiphase flow., in: *Proceedings of the 9th International Conference on Machine Learning and Computing*, 2017, pp. 141–146.
- [9] S. Mishra, A. Datta-Gupta, *Applied Statistical Modeling and Data Analytics - A Practical Guide for the Petroleum Geosciences*, Elsevier, 2018.
- [10] T. A. AL-Qutami, R. Ibrahim, I. Ismail, Virtual multiphase flow metering using diverse neural network ensemble and adaptive simulated annealing, *Expert Systems With Applications* 93 (2018) 72–85.
- [11] M. M. Câmara, R. M. Soares, T. Feital, T. K. Anzai, F. C. Diehl, P. Thomson, J. Pinto, Numerical aspects of data reconciliation in industrial applications, *Processes* 5 (2017).
- [12] Y. Gal, *Uncertainty in Deep Learning*, PhD thesis, University of Cambridge (2016).

- [13] T. A. AL-Qutami, R. Ibrahim, I. Ismail, M. A. Ishak, Development of soft sensor to estimate multiphase flow rates using neural networks and early stopping, in: *International Journal on Smart Sensing and Intelligent Systems*, Vol. 10, 2017, pp. 199–222.
- [14] G. Zangl, R. Hermann, S. Christian, Comparison of methods for stochastic multiphase flow rate estimation, *SPE Annual Technical Conference and Exhibition 12* (2017).
- [15] O. Bello, S. Ade-Jacob, K. Yuan, Development of hybrid intelligent system for virtual flow metering in production wells, in: *SPE intelligent energy conference & exhibition*, Society of Petroleum Engineers, 2014.
- [16] L. Xu, W. Zhou, X. Li, S. Tang, Wet gas metering using a revised venturi meter and soft-computing approximation techniques, *IEE transactions on instrumentation and measurement* 60 (2011) 947–956.
- [17] T. Bikmukhametov, J. Jäschke, Oil Production Monitoring Using Gradient Boosting Machine Learning Algorithm, *IFAC-PapersOnLine* 52 (2019).
- [18] S. M. Berneti, M. Shahbazian, An imperialist competitive algorithm - artificial neural network method to predict oil flow rate of the wells, *International Journal of Computer Applications* 26 (2011) 47–50.
- [19] M. A. Ahmadi, M. Ebadi, A. Shokrollahi, S. M. J. Majidi, Evolving artificial neural network and imperialist competitive algorithm for prediction oil flow rate of the reservoir, *Applied Soft Computing* 13 (2013) 1085–1098.
- [20] M. Z. Hasanvand, S. Berneti, Predicting oil flow rate due to multiphase flow meter by using an artificial neural network, *Energy Sources Part A Recovery Utilization and Environmental Effects* 37 (2015) 840–845.
- [21] T. A. AL-Qutami, R. Ibrahim, I. Ismail, M. A. Ishak, Hybrid neural network and regression tree ensemble pruned by simulated annealing for virtual flow metering application, in: *IEEE International Conference on Signal and Image Processing Applications (ICSIPA)*, 2017, pp. 304–309.
- [22] H. P. Bieker, O. Slupphaug, T. A. Johansen, Well management under uncertain gas or water oil ratios, in: *Digital Energy Conference and Exhibition*, Society of Petroleum Engineers, 2007.
- [23] J. R. Fonseca, M. Gonçalves, L. Azevedo, Consideration of uncertainty in simulation and flow. In Portuguese: Consideração de incerteza nas simulações de elevação e Escoamento, in: *An. do IV Semin. Elev. Artif. e Escoamento*, 2009.
- [24] D. D. Monteiro, G. S. Chaves, V. M. F. Filho, J. S. Baioco, Uncertainty analysis for production forecast in oil wells, in: *SPE Latin American And Caribbean Petroleum Engineering Conference*, 2017.

- [25] Z. Ghahramani, Probabilistic machine learning and artificial intelligence, *Nature, suppl. Insight: Machine Intelligence* 521 (2015) 452–459.
- [26] T. Hastie, R. Tibshirani, J. Friedman, *The Elements of Statistical Learning*, Springer, New York, USA, 2009.
- [27] R. J. Lorentzen, A. S. Stordal, G. Nævdal, H. A. Karlsen, H. J. Skaug, Estimation of production rates with transient well-flow modeling and the auxiliary particle filter, *Society of Petroleum Engineers* 19(1) (2014) 172–180.
- [28] R. J. Lorentzen, A. S. Stordal, X. Luo, G. Nævdal, Estimation of production rates by use of transient well-flow modeling and the auxiliary particle filter: Full-scale applications, *SPE Production and Operations* 31(2) (2016) 163–175.
- [29] X. Luo, R. J. Lorentzen, A. S. Stordal, G. Nævdal, Toward an enhanced Bayesian estimation framework for multiphase flow soft-sensing, *Inverse Problems* 30 (2014).
- [30] R. G. Nastaran Bassamzadeh, Probabilistic data-driven prediction of well-bore signatures in high-dimensional data using bayesian networks, *Society of Petroleum Engineers* (2018).
- [31] N. G. Polson, V. Sokolov, Deep learning: A Bayesian perspective, *Bayesian Analysis* 12 (4) (2017) 1275–1304.
- [32] J. Snoek, H. Larochelle, R. P. Adams, Practical Bayesian Optimization of Machine Learning Algorithms, *arXiv preprints*, arXiv:1206.2944v2 (2012).
- [33] D. M. Blei, A. Kucukelbir, J. D. McAuliffe, Variational Inference: A Review for Statisticians, *Journal of the American Statistical Association* 112 (518) (2017) 859–877.
- [34] Y. Liu, Q. Liu, W. Wang, J. Zhao, H. Leung, Data-driven based model for flow prediction of steam system in steel industry, *Information Sciences* 193 (2012) 104–114.
- [35] G. B. Humphrey, M. S. Gibbs, G. C. Dandy, H. R. Maier, A hybrid approach to monthly streamflow forecasting: Integrating hydrological model outputs into a Bayesian artificial neural network, *Journal of Hydrology* 540 (2016) 623–640.
- [36] S. Corneliussen, J.-P. Couput, E. Dahl, E. Dykesteen, K.-E. Frøysa, E. Malde, H. Moestue, P. O. Moksnes, L. Scheers, H. Tunheim, *Handbook of multiphase flow metering*, The Norwegian Society for Oil and Gas Measurements, 2005.
- [37] C. Marshall, A. Thomas, Maximising economic recovery - a review of well test procedures in the north sea, in: *Offshore Europe Conference and Exhibition*, Society of Petroleum Engineers, 2015.

- [38] K. Krejbjerg, N. Lindeloff, H. Berentsen, V. R. Midttveit, Conversion of multiphase meter flowrates, The Norwegian Society for Oil and Gas Measurements, NFOGM (2019).
- [39] B. Grimstad, V. Gunnerud, A. Sandnes, S. Shamlou, I. S. Skrondal, V. Uglane, S. Ursin-Holm, B. Foss, A Simple Data-Driven Approach to Production Estimation and Optimization, in: SPE Intelligent Energy International Conference and Exhibition, Society of Petroleum Engineers, 2016.
- [40] A. M. Woodward, B. K. Alsberg, D. B. Kell, The effect of heteroscedastic noise on the chemometric modelling of frequency domain data, *Chemometrics and Intelligent Laboratory Systems* 40 (1998) 101–107.
- [41] X. Glorot, Y. Bengio, Understanding the difficulty of training deep feedforward neural networks, in: *Journal of Machine Learning Research*, Vol. 9, 2010, pp. 249–256.
- [42] K. He, X. Zhang, S. Ren, J. Sun, Delving Deep into Rectifiers: Surpassing Human-Level Performance on ImageNet Classification, in: *Proceedings of the IEEE international conference on computer vision*, 2015, pp. 1026–1034.
- [43] D. P. Kingma, M. Welling, Auto-Encoding Variational Bayes, in: *2nd International Conference on Learning Representations (ICLR)*, 2014.
- [44] C. Blundell, J. Cornebise, K. Kavukcuoglu, D. Wierstra, Weight Uncertainty in Neural Networks, in: *32nd International Conference on Machine Learning*, Vol. 37, 2015, pp. 1613–1622. arXiv:1505.05424.
- [45] D. P. Kingma, T. Salimans, M. Welling, Variational dropout and the local reparameterization trick, in: *Advances in Neural Information Processing Systems* 28, Curran Associates, Inc., 2015, pp. 2575–2583.
- [46] X. Glorot, A. Bordes, Y. Bengio, Deep Sparse Rectifier Neural Networks, in: *Proceedings of the Fourteenth International Conference on Artificial Intelligence and Statistics*, Vol. 15, 2011, pp. 315–323.
- [47] Y. Bengio, Practical recommendations for gradient-based training of deep architectures, in: *Neural networks: Tricks of the trade*, Springer, 2012, pp. 437–478.
- [48] D. P. Kingma, J. L. Ba, Adam: A method for stochastic optimization, in: *3rd International Conference on Learning Representations, ICLR 2015*, 2015, pp. 1–15.
- [49] I. Goodfellow, Y. Bengio, A. Courville, *Deep Learning*, MIT Press, 2016.